ADVANCED MATERIALS INTERFACES
www.advmatinterfaces.de

Coupling Diffusion Welding Technique and Mesh Screen Creates Heterogeneous Metal Surface for Droplets Array

Jian Xie, Jinliang Xu, Qi Liu, and Xiang Li*

Nonsilicon micromachining is a challenge, especially for large scale heterogeneous (hydrophilic/hydrophobic) surface fabrication. Here, mesh screen and diffusion welding technique are coupled to form a novel fabrication method. Mesh screen is used as mask. The diffusion welding technique sinters mesh screen on copper surface to form welding junction array. Chemical treatment of sintered package forms superhydrophobic nanostructures on surfaces except welding junction array. Separating mesh screen from copper substrate exposes hydrophilic dots array, corresponding to welding junction array. Thus, heterogeneous surface is created. By condensing wet air, main droplet and neighboring droplet occur on hydrophilic dot and superhydrophobic part, respectively. For horizontal surface, neighboring droplets initially generated on nanograsses behave consecutive events of coalescence, jump, and return, triggering contact/noncontact effect induced jumping. Thus, defect droplet area is formed and droplet size uniformity is broken. A nondimensional equation is proposed for the contact effect induced jumping analysis. Noncontact effect induced jumping is found for the first time. For vertical surface, droplet array behaves monodisperse size due to departure of merged neighboring droplets without returning, and equal opportunities of neighboring droplets captured by main droplets. The work opens a new way for large scale droplet array generation by controllable condensation.

1. Introduction

Condensing droplets on hydrophobic surface have a wide range of size distribution.[1] The distances between droplets vary too much. Many factors influence droplet size distribution. Droplet nucleation is a random behavior.[2] Even for an ordered nanostructured surface, it is impossible to nucleate liquid droplets simultaneously. Droplets have different sizes due to different time history of droplet growth.[3] Droplets coalescence creates larger droplet than not merged. Droplet size distribution is important to influence thermal performance of heat exchangers.[4]

Droplet arrays with monodisperse size and ordered pattern should be satisfied to reach "*one cell, one well*" target.[5] For biology application, Zhu et al. reported a nanoliter droplet array to quantify gene expression in individual cells.[6] By sequentially printing nanoliter-scale droplets on a microfluidic robot, all liquid-handling operations can be automatically achieved.[7–9] For optical application, droplet-based microfluidic system was used to obtain lens arrays by using a thin liquid layer on a polar electric crystal like $LiNbO_3$.[10] For electronic application, liquid metal droplet array is used as a capacitive-type touch sensor.[11]

Usually, heterogeneous surface with ordered hydrophilic islands/cavities on hydrophobic area is the key to confine liquids to form droplet array.[12,13] To fabricate a heterogeneous surface, a uniformly hydrophobic surface was generated first. Various methods are available for surface hydrophobicity. Then, a mask was prepared for selective etching to create hydrophilic islands/cavities. Ultraviolet light,[14–17] X-ray,[18] laser,[19] and plasma[8,20,21] can be used for etching, which should match the hydrophobic surface behavior. For example, the ultraviolet light can etch hydrophobic surface with ZnO nanostructure due to their photo catalytic degradation nature.[17]

It is noted that masks are fabricated by microelectrical mechanical systems (MEMS) using silicon wafer. Heterogeneous surface size is limited by silicon wafer with a typical size of 4 inches. The etching technique not only has high cost but also is not suitable for large scale utilization. An emerging area using heterogeneous surface to produce droplets pattern is the mechanical engineering. Yoo et al. noted that water droplets on a piece of metallic surface can absorb electromagnetic wave, which is attractive for military fighter, tank, and warship to avoid radar detection.[22] For environment protection, it is difficult to collect ultrafine dust particles from a large air volume. An idea was proposed to absorb fine particles by electriferous droplet array.[23] For these applications, large area heterogeneous surface in ≈m^2 scale should be fabricated on metal substrate with acceptable cost.

We proposed a novel method to create metal based heterogeneous surface for controllable condensing droplets arrays. Mesh screen is used as mask. The *diffusion welding technique* in metallurgy area is introduced here. The fabrication principle adjoining mesh screen and diffusion welding technique was carefully described. The observed droplet dynamics and a theoretical

---

Dr. J. Xie, Prof. J. Xu, Q. Liu, X. Li
The Beijing Key Laboratory of Multiphase Flow and Heat Transfer
for Low Energy Utilization
North China Electric Power University
Beijing 102206, P. R. China
E-mail: xjl@ncepu.edu.cn

The ORCID identification number(s) for the author(s) of this article can be found under https://doi.org/10.1002/admi.201700684.

DOI: 10.1002/admi.201700684

model for horizontally positioned surface were reported to explain the poor quality of droplet array formation. Perfect droplet array on vertically positioned surface was demonstrated, which is expected for large scale utilization.

2. Results and Discussion

2.1. The Heterogeneous Metal Surface

The original contribution of this paper is to combine the diffusion welding technique and mesh screen to fabricate heterogeneous surface. Using diffusion welding technique or mesh screen alone cannot reach such target. Diffusion welding technique is used to weld different materials such as nickel and molybdenum/copper joints.[24] The two parts to be welded use either bulk or film materials.[25,26] Pore structure is seldom considered to be welded. Mesh screen has pore structure which has been used for wicking in heat pipes,[27] collection of droplets in fog,[28] separation of oil–water mixture,[29,30] etc. It is not used as mask for material fabrication. In this study, welding mesh screen on metal substrate forms hydrophilic microdot array. Pores in mesh screen allow the surface except microdot array to be immersed in chemical solution, forming hydrophobic nanograsses.

Figure 1a shows tinbronze mesh screen used here. Mass concentration of tin element was 6.15–7.79% based on energy dispersive spectrometer measurement. The mesh screen had d = 41 µm (wire thickness) and w = 62 µm (pore width). The substrate was pure cooper. After sintering, the whole package was immersed in chemical solution. Even though the mesh screen was oxidized (see Figure S1, Supporting Information), it prevented welding junction arrays from oxidization. Much attention was paid to heterogeneous surface after removing mesh screen (see Figure 1b). Four microdots form one unit. Distance between neighboring dots is expressed as $P = \sqrt{2}(w + d)$. Here, P is 146 µm with w = 62 µm and d = 41 µm. Figure 1c,d shows superhydrophobic nanograsses and hydrophilic microdot. Microdot is ellipse with a horizontal axis length of a = 47 µm and a vertical axis length of b = 22 µm. Several micropits exist in a dot. Each pit had a sphere particle coming from tin element embedded in mesh screen, induced by diffusion welding technique.

Experimental setup can be seen in the Supporting Information. We demonstrate droplet dynamics on the heterogeneous surface. Practically, any droplet has 3D motion. Achieving 3D velocities of a droplet is difficult. The 3D to 2D conversion of droplet velocities is fulfilled by ensuring image files in focus plane of the high speed camera. Image files are on X–Y plane (focus plane), with a pixel resolution of δ. Within a time step Δt, pixel locations of the droplet are at (M_t, N_t) at time t and $(M_{t-\Delta t}, N_{t-\Delta t})$ at time $t - \Delta t$, where M and N are the pixel number in X and Y coordinate, respectively. Thus, velocities are $u_X = (M_t - M_{t-\Delta t})\delta/\Delta t$, $u_Y = (N_t - N_{t-\Delta t})\delta/\Delta t$. Thus, the absolute velocity is $u = \sqrt{u_X^2 + u_Y^2}$.

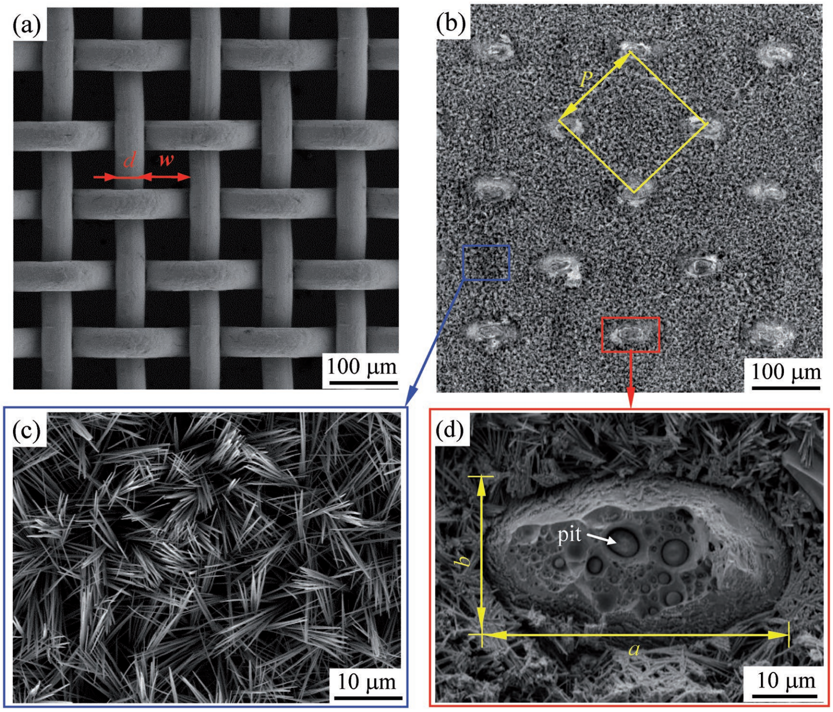

Figure 1. The structure of mesh screen and heterogeneous surface: a) mesh screen; b) heterogeneous surface; c) hydrophobic nanograsses; d) microhydrophilic dot with a = 47 µm, b = 22 µm, and P = 146 µm.

2.2. Observed Droplet Dynamics on Horizontal Surface

Droplets are preferred to be nucleated and growing on hydrophilic dot. Contact area between droplet and solid material is specified at the hydraulic/hydrophobic interface. Contact angles are continuously increased versus time. This process is stopped until contact angle reaches the advancing value, beyond which the contact area expands. Droplets on hydrophilic dots and hydrophobic area are called main and neighboring droplets, respectively.

Figure 2 shows consecutive images of condensing droplets on horizontal surface. Main droplet array is formed. Each main droplet corresponds to a specific hydrophilic dot. Main droplets become larger versus time. Neighboring droplet on hydrophobic area is one to two orders magnitude smaller than main droplet. Main droplet array is not perfect due to two reasons: (1) some larger main droplets than others (see Figure 2c) and (2) defect droplet area due to disappearance of some main droplets (see Figure 2h).

Figure 3 shows side view droplet trajectories coming from Videos S2–S6 in the Supporting Information. **Figure 4** plotted 3D drawing for droplet dynamics. Figures 3 and 4 explained nonuniform main droplet size and defect droplet area observed in Figure 2. Available studies dealt with coalescence induced jumping for droplets initially on solid surface.[31–38] Here, a returning droplet impacting droplets on the solid surface was paid attention (see Figure 4b). After impacting, five cases are classified:

Case 1—Stabilized Droplet after Coalescence: Figures 3a and 4c show a returning droplet impacting a larger droplet on a

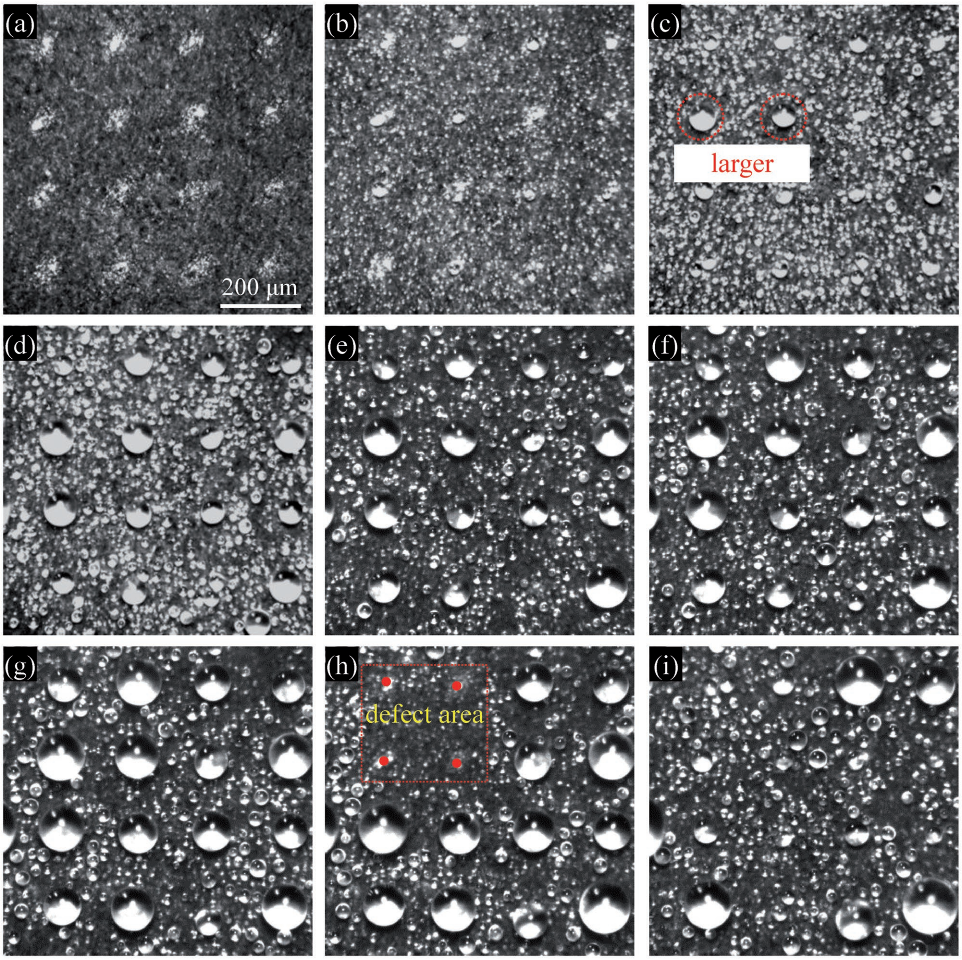

Figure 2. Droplet growth and pattern on horizontal heterogeneous surface (note that all panels have identical scale bar and time difference Δt is 2 min between consecutive images; see Video S1, Supporting Information).

hydrophilic dot. After coalescence, the merged droplet did not jump and stayed on the hydrophilic dot, explaining larger droplet size on such location than others (see Figure 2c).

Case 2—Single Time Droplets Coalescence Induced Jumping: Different from case 1, Figures 3b and 4d demonstrate the merged droplet successfully escaped from hydrophilic dot to yield defect droplet area (see Figure 2h).

Case 3—The Domino Effect of Droplets Coalescence and Jumping: Coalescence induced jumping can be repeated for several times to form domino effect (see Figures 3c and 4e). A previous jumping droplet becomes the seeding droplet to trigger a new turn of coalescence and jumping. For the current turn compared with the previous turn, the flying droplet is larger and can also jump much higher. Luo et al.[39] and Lv et al.[40] found similar phenomenon. In this study, the domino effect causes severe defect droplets area.

Case 4—Droplet Jumping Triggered by Rotating-Droplet-Induced-Gas-Disturbance: When a returning droplet impacts a main droplet tangentially, coalescence yields the merged droplet rotating. The nearby wet air is being sheared to have a rotating flow field, triggering a nearby droplet jumping (see Figures 3d and 4f).

Case 5—Droplet Jumping Triggered by the Billiard Effect: When a returning droplet impacts a main droplet on a hydrophilic dot, a nearby droplet is being triggered to jump by the gas turbulence at a specific angle with respect to the incoming seeding droplet trajectory, similar to a billiard movement (see Figures 3e and 4g).

Cases 2 and 3 belong to the coalescence induced droplet jumping, we call it as the contact effect induced droplet jumping. Cases 4 and 5 involve the droplet jumping by gas disturbance, we call it as the noncontact effect induced droplet jumping, which is reported here for the first time. We note that, for cases 2 and 3, each impacting creates a single seeding droplet leaving the surface. However, for cases 4 and 5, each impacting may create several seeding droplets, which can severely destroy the self-organization of droplets array.

2.3. Theoretical Model of the Droplet Dynamics

This section theoretically explains: (1) droplet jumping/not jumping after coalescence and (2) increased jumping height for specific turn than previous turn. The problem is described using nondimensional parameters to provide

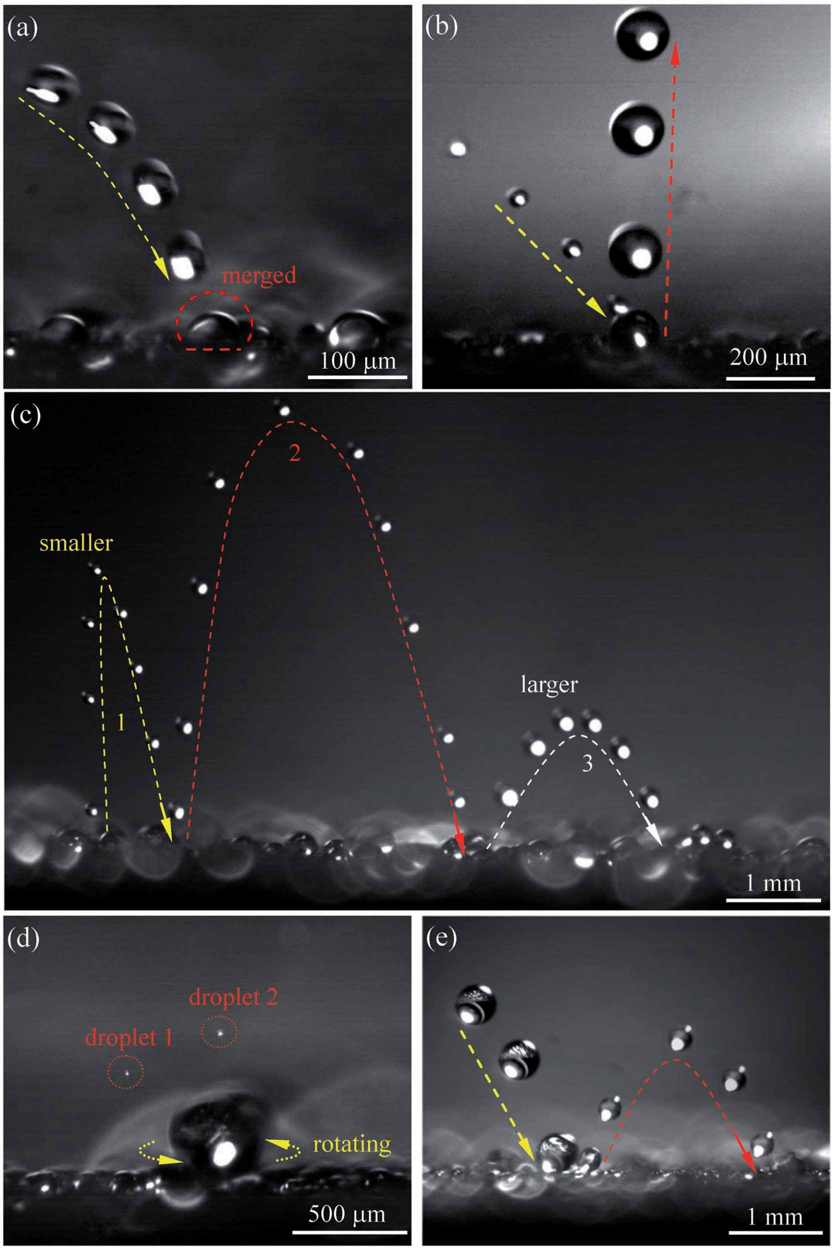

Figure 3. Droplet return induced dynamics: a) a return droplet with radius of 19.9 μm and velocity of 57 mm s^{-1} impacts a main droplet with radius of 30.1 μm and CA of 123.7°, the merged droplet has a radius of 37.5 μm and CA of 138.8°, $\Delta t = 2.0$ ms; b) a return droplet with radius of 24.2 μm and velocity of 99 mm s^{-1} impacts a 56.7 μm radius droplet (CA = 155.6°), inducing the merged droplet jumping with radius of 61.2 μm and velocity of 162 mm s^{-1}, $\Delta t = 2.0$ ms; c) the droplet return and coalescence triggered domino effect; d) the neighboring droplet jumping triggered by rotating-droplet-induced-gas-disturbance; e) the billiard effect induced droplet jumping by the droplet sweeping disturbance, see Videos S2–S6, Supporting Information, corresponding to (a)–(e).

a general analysis. **Figure 5** shows the physical model. A returning droplet with a radius of r_0 impacts several droplets on a surface simultaneously (see Figure 5a). The impacting velocity is u_0. Droplets on the surface are recorded as $1 \cdots i \cdots N$, with radiuses of $r_1 \cdots r_i \cdots r_N$ and contact angles of $\theta_1 \cdots \theta_i \cdots \theta_N$, respectively. After coalescence, the jumping velocity is u_c, the mass conservation yields the radius of r_c as (see Figure 5b)

$$r_c = \sqrt[3]{r_0^3 + \frac{1}{4}\sum_{i=1}^{i=N}\left[r_i^3\left(1-\cos\theta_i\right)^2\left(2+\cos\theta_i\right)\right]} \qquad (1)$$

The residue kinetic energy $E_{k,c}$ characterizes how much energy can be converted into kinetic energy after coalescence. The merged droplet cannot jump if $E_{k,c} < 0$. The energy conservation yields

$$E_{k,c} = E_{k,0} + \Delta E_s + \Delta E_h - E_{vis} \qquad (2)$$

where $E_{k,0}$ is the kinetic energy of the seeding droplet before coalescence, ΔE_s is the difference of surface energy before and after coalescence, ΔE_h is the gravity potential energy due to the variation of center mass of droplets before and after coalescence, ΔE_{vis} is the viscous dissipation during coalescence. $E_{k,0}$ and $E_{k,c}$ are

$$E_{k,0} = \frac{2}{3}\pi\rho r_0^3 u_0^2, \quad E_{k,c} = \frac{2}{3}\pi\rho r_c^3 u_c^2 \qquad (3)$$

where ρ is the liquid density. Liu et al.[41] divided the whole process into two substages of coalescence and departure. Adhesion work was introduced in the later stage. Physically, adhesion work is the difference of surface energy due to solid–liquid interface before droplet departure replaced by gas–solid interface on solid surface, and gas–liquid interface on droplet, after droplet departure. A final droplet with a spherical cap and a flat bottom interface is considered to treat adhesion work, deviating from practical sphere droplet. Instead, ΔE_s is used to treat the surface energy difference, similar to the treatment of Kim et al.[42] ΔE_s is

$$\Delta E_s = 4\pi\sigma\left(r_0{}^2 - r_c^2\right) + 2\pi\sigma\sum_{i=1}^{i=N}\left[r_i{}^2(1-\cos\theta_i)\right] + (1-\varphi_s-\varphi_s\cos\theta_Y)\pi\sigma\sum_{i=1}^{i=N}\left(r_i{}^2\sin^2\theta_i\right) \qquad (4)$$

where σ is the surface tension force and θ_Y is the characteristic contact angle. We note that Equation (4) is a general expression to consider micro/nanoroughness effect. The parameter φ_s considers wetting behavior and surface roughness effect, which is the ratio of solid–liquid contact area (including wetted regions inside roughness) to contact area between droplet and a flat surface. Relative roughness r_s is the extended surface area of micro/nanostructure divided by the flat surface area. Three cases are considered (see Figure S3,

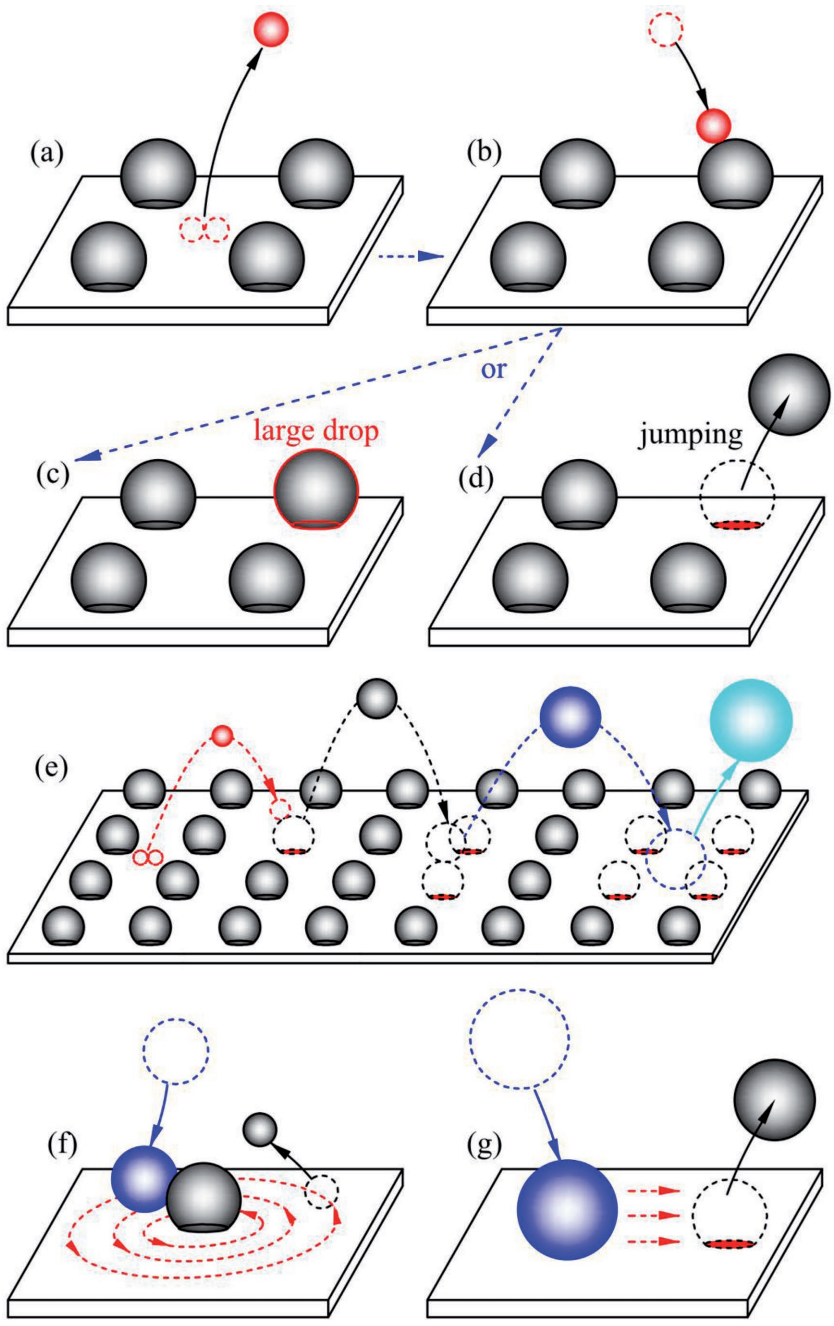

Figure 4. The mechanisms explaining nonuniform droplet size and defect droplet area.

Supporting Information). For partial wetting, φ_s is smaller than r_s. For complete wetting, φ_s equals r_s. We study a returning droplet impacting a droplet on microhydrophilic dot, which is sufficiently smooth compared with nanostructure to yield $\varphi_s = r_s \approx 1$. ΔE_h is

$$\Delta E_h = \frac{4}{3}\pi\rho g\left(r_0^4 - r_c^4\right) + \frac{\pi}{12}\rho g\sum_{i=1}^{i=N}\left[r_i^4\left(1-\cos\theta_i\right)^3\left(3+\cos\theta_i\right)\right] \tag{5}$$

where g is the gravity acceleration, ΔE_{vis} is

$$E_{vis} = 3\pi\kappa\mu\sqrt{\frac{\sigma r_0^3}{\rho}} + \sum_{i=1}^{i=N}\left[\frac{12\kappa\mu\left(\theta_i - \sin\theta_i\cos\theta_i\right)^2}{\pi\left(1-\cos\theta_i\right)^2\left(2+\cos\theta_i\right)}\sqrt{\frac{\sigma r_i^3}{\rho}}\right] \tag{6}$$

where μ is the liquid viscosity. Combining Equations (1)–(6) and introducing nondimensional parameters yield

$$\frac{2}{3}\left(1-\beta_0^3\xi^2\right)We = 4\left(\beta_0^2-1\right) + \sum_{i=1}^{i=N}\beta_i^2\Psi(\theta_i) - \left(3\kappa + \sum_{i=1}^{i=N}\beta_i^{3/2}\Pi(\theta_i)\right)Oh + \left(\beta_0^4 + \frac{1}{12}\sum_{i=1}^{i=N}\beta_i^4\Omega(\theta_i) - \frac{4}{3}\right)Bn \tag{7}$$

where We, Oh, and Bn are Weber number, Ohnesorge number, and Bond number, respectively. They are

$$We = \frac{\rho r_c u_c^2}{\sigma},\quad Oh = \frac{\mu}{\sqrt{\rho r_c \sigma}},\quad Bn = \frac{\rho g r_c^2}{\sigma} \tag{8}$$

In Equation (7), $\beta_0 = r_0/r_c$, $\beta_i = r_i/r_c$, $\xi = u_0/u_c$. $\Psi(\theta_i)$, $\Pi(\theta_{i,})$, and $\Omega(\theta_i)$ are

$$\Psi(\theta_i) = 2 - 2\cos\theta_i + \left(1-\varphi_s-\varphi_s\cos\theta_Y\right)\sin^2\theta_i \tag{9}$$

$$\Pi(\theta_i) = \frac{12\kappa\left(\theta_i-\sin\theta_i\cos\theta_i\right)^2}{\pi^2\left(1-\cos\theta_i\right)^2\left(2+\cos\theta_i\right)} \tag{10}$$

$$\Omega(\theta_i) = \left(1-\cos\theta_i\right)^3\left(3+\cos\theta_i\right) \tag{11}$$

Equation (7) is a general expression. Specifically, it is suitable for all droplets on the surface without returning droplet involved ($u_0 = 0$ and $r_0 = 0$),[43] a returning droplet impacting a single ($N = 1$) or multidroplets ($N > 1$)[42] on the surface. We consider a returning droplet impacting a single droplet, Equation (7) becomes

$$\frac{2}{3}\left(1-\beta_0^3\xi^2\right)We = 4\left(\beta_0^2-1\right) + \beta_1^2\Psi(\theta_1) - \left(3\kappa + \beta_1^{3/2}\Pi(\theta_1)\right)Oh + \left(\beta_0^4 + \frac{1}{12}\beta_1^4\Omega(\theta_1) - \frac{4}{3}\right)Bn \tag{12}$$

Equation (12) was used to analyze the effect of r_0 and u_0 on u_c, including the case of Figure 3b. Droplet grows according to constant contact area between droplet and surface with varied

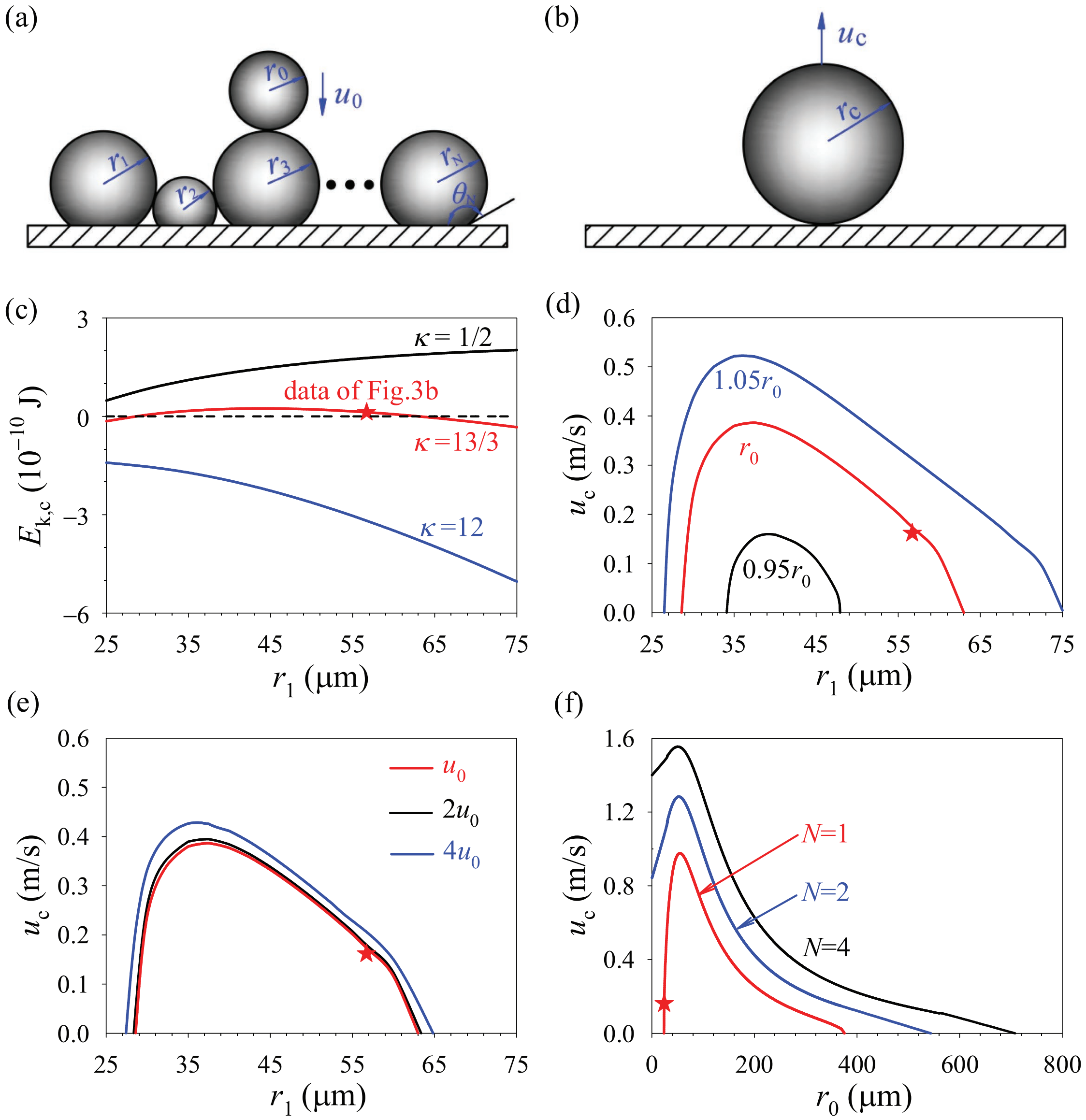

Figure 5. Droplet dynamics on horizontal heterogeneous surface: a) droplets just before impacting; b) droplet after coalescence; c) $E_{k,c}$ versus r_1 with u_0 and r_0 from Figure 3b; d) u_c versus r_1 at $u_0 = 99$ mm s^{-1} and $1.05r_0$, r_0 and $0.95r_0$ ($r_0 = 24.2$ μm); e) u_c versus r_1 at $r_0 = 24.2$ μm and u_0, $2u_0$, and $4u_0$ ($u_0 = 99$ mm s^{-1}); f) u_c versus r_0 at $u_0 = 99$ mm s^{-1}, $r_i = 56.7$ μm, and $N = 1$, 2, and 4, respectively.

contact angles.[44] Droplet radius r_1 is written as $r_1 = \frac{a}{2\sin\theta_1}$, where a is the horizontal axial length of hydrophilic dot (a = 47 μm in Figure 1d), other properties are $\rho = 999$ kg m^{-3}, $\mu = 1.001 \times 10^{-3}$ Pa s, $\sigma = 0.072$ N m^{-1}, and $\varphi_s = 1$. Various κ values are suggested in the literature. It is not acceptable for $\kappa = 0$. Lv et al.[40,45] assumed that velocity gradient only exists in the droplet height direction during coalescence and suggested $\kappa = 1/2$. Most of studies[33,41,43] considered velocity gradient existing in 3D and used $\kappa = 12$. Aili et al.[46] suggested $\kappa = 13/3$ based on their experimental data.

Figure 5c shows $E_{k,c}$ versus r_1 with $r_0 = 24.2$ μm and $u_0 = 99$ mm s^{-1} (r_0 and u_0 are from Figure 3b). The κ values of 1/2, 13/3, and 12 are used. It is found that $\kappa = 13/3$ matched our experimental data well. The effect of r_1 on jumping velocity u_c is plotted in Figure 5d with three returning droplet radiuses of $1.05r_0$, r_0, and $0.95r_0$. For specific r_0 and u_0, u_c displays quasi-parabola shape versus r_1. Droplet on the surface has a specific size range within which the merged droplet can jump, but beyond which the merged droplet cannot jump. For example, a returning droplet of $r_0 = 24.2$ μm can lift a maximum droplet of $r_1 = 63.0$ μm on the surface (red curve in Figure 5d). For $u_0 = 99$ mm s^{-1}, $r_0 = 24.2$ μm, and $r_1 = 56.7$ μm, the computed u_c is 175 mm s^{-1}, approaching the measured value of 162 mm s^{-1} (see red star symbol in Figure 5d). The maximum u_c at $r_1 = 37.5$ μm is 386 mm s^{-1}, almost four times of u_0. The seeding droplet size r_0 significantly influences the droplet size range that can be lifted. A slight increase of r_0 (for example, 5% larger), apparently enlarges the r_1 range and increases the maximum u_c. However, Figure 5e shows the insensitive effect of impacting velocities u_0

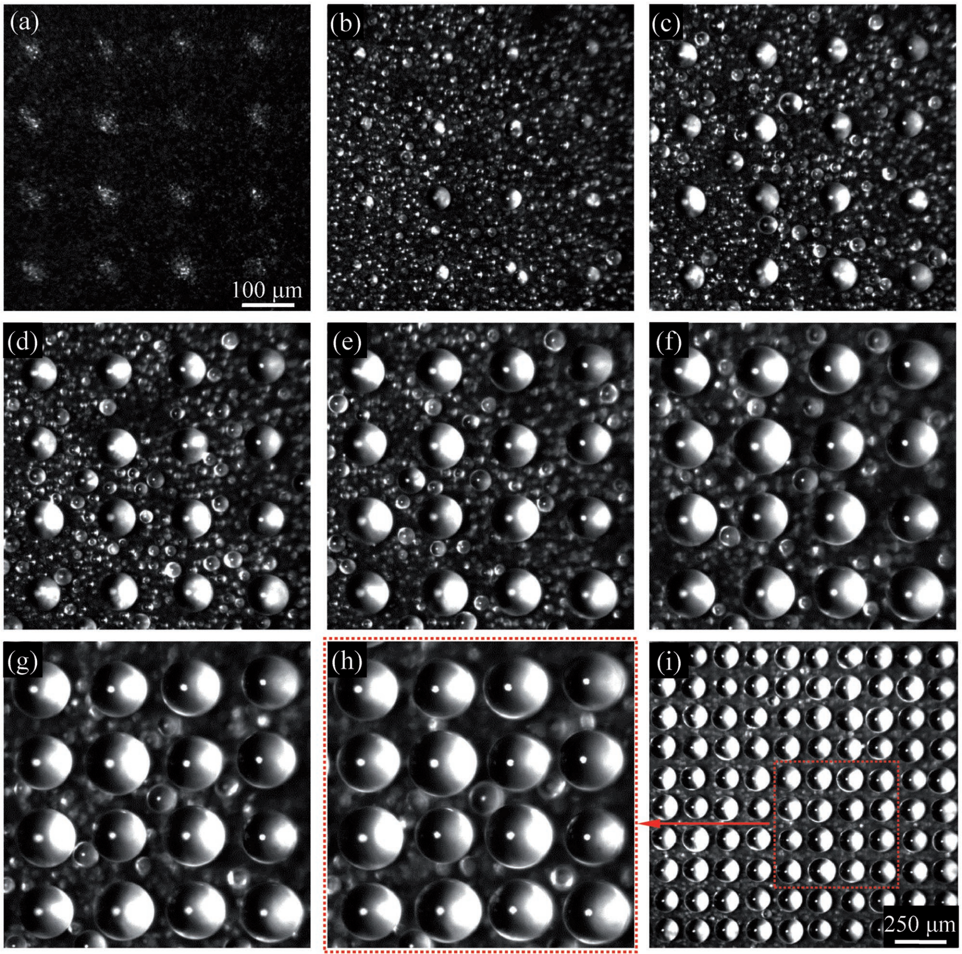

Figure 6. The formation of perfect main droplet array on vertical heterogeneous surface (note that panels (a)–(h) have identical scale bar as shown in (a), panel (i) has the scale bar of 250 µm, and time difference is 3 min between consecutive images; see Video S7, Supporting Information).

on $u_c \approx r_1$ curves. The surface energy and viscous dissipation are competed with each other to yield the quasi-parabola curve. Under specific condition, a smaller seeding droplet can lift a larger droplet on the surface, and/or the jumping velocity can be significantly larger than the impacting velocity. The release of surface energy, not the kinetic energy of the seeding droplet, provides the energy to lift a larger droplet, or to create a larger jumping velocity. For $u_0 = 99$ mm s^{-1} and $r_1 = 56.7$ µm, Figure 5f demonstrates the seeding droplet impacting single or multidroplets (N = 1, 2, and 4). The multidroplets coalescence apparently enlarges the seeding droplet size range r_0 and maximum jumping velocity u_c.

We talk about the domino effect of droplets coalescence and jumping. The time scale for multitimes jumping is significantly shorter than that of condensation heat transfer. During domino process, droplets on surface remain constant size, but the seeding droplet size is increased due to coalescence. Figure 5f told us that when a seeding droplet is large enough, it cannot lift a droplet on the surface to terminate the domino effect. Even though the domino effect can be finally stopped, it caused defect droplet areas on a set of locations.

2.4. Ordered Droplets Pattern on Vertical Heterogeneous Surface

Ordered droplets pattern was achieved on vertical heterogeneous surface. **Figure 6** shows growing droplets with uniform size. Defect droplets area was not observed. Droplet density n is determined by the distance of hydrophilic dots P (see Figure 1b), which is $n = 1/P^2$. Here, n is 47 mm^{-2}, corresponding to Figure 6i. Main droplets have narrow size range to display monodisperse characteristic (see Figure S4, Supporting Information). The deviation parameters of e_R, e_A, and e_n cited from ref. [47] characterized droplet size deviation. The smaller the deviation, the more uniform of droplet size is. For visualized droplets in Figure 6i, e_R, e_A, and e_n are −0.08%, 3.64%, and 4.83%, respectively. **Figure 7** shows neighboring droplets coalescence and jumping (see Video S8, Supporting Information). **Figure 8** illustrates two mechanisms to keep uniform size of main droplets.

Equal Capture Opportunity of Neighboring Droplets by Main Droplets: Under main droplets, a neighboring droplet is growing to be captured by a main droplet (see case 1 in Figure 8b). Alternatively, coalescence induced jumping of two or more

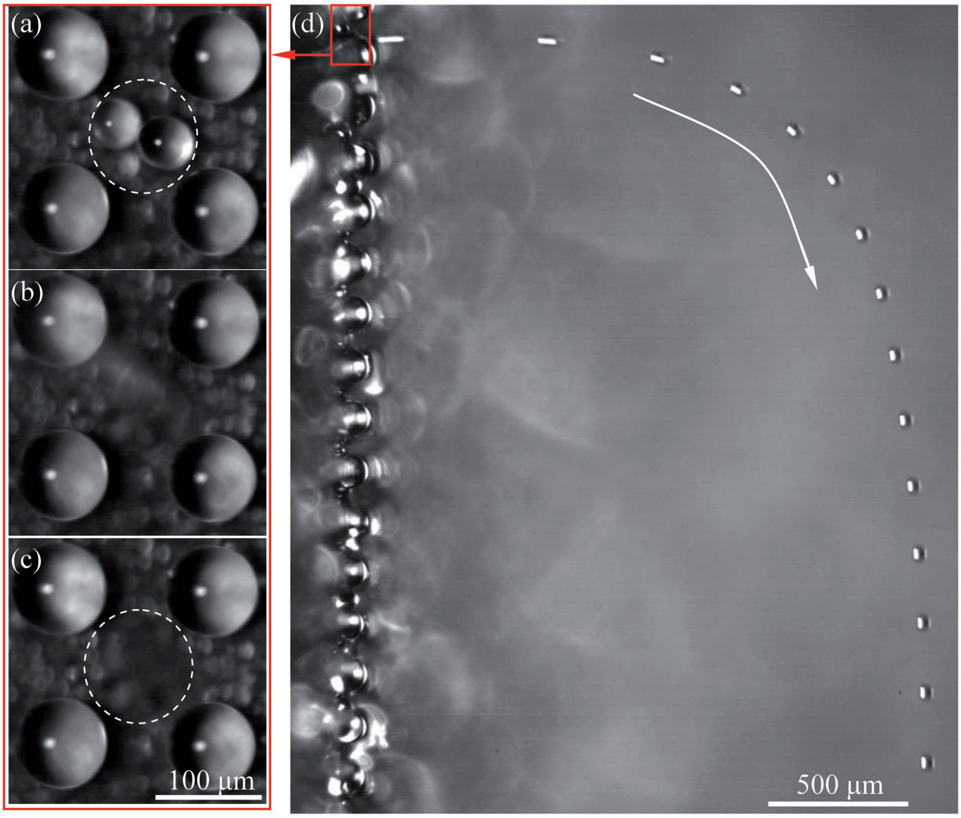

Figure 7. The neighboring droplets coalescence and jumping without returning (note that panels (a)–(c) have identical scale bar and time difference is 2 ms between neighboring images from (a) to (c); see Video S8, Supporting Information).

neighboring droplets yields the capture by a main droplet (see case 2 in Figure 8b). Even though neighboring droplets display random behavior on hydrophobic part, the capture opportunities are identical for all main droplets (see Figure 8c).

Successful Departure of Merged Neighboring Droplets Not Under Main Droplets: After coalescence of neighboring droplets not under main droplets, the merged droplet departs from the surface without returning. Such process does not influence main droplet size (see case 3 in Figure 8b).

When main droplets diameters approach the distance of hydrophilic dots P (see Figure 8d), large scale coalescence and jumping happens (see Figure S5 and Video S9, Supporting Information). Considering this criterion, let $u_0 = 0$, $r_0 = 0$, $r_i = 0.5P$, and $\theta_i = \arcsin(a/P) = 161°$, Equation (7) gives

$$u_c = \sqrt{\frac{12(\beta_0{}^2 - 1) + 3N\sum_{i=1}^{i=N}\beta_i{}^2\Psi(\theta_i) - \left(9\kappa + 3N\sum_{i=1}^{i=N}\beta_i{}^{3/2}\Pi(\theta_i)\right)Oh}{2\left(1 - \beta_0{}^3\xi^2\right)}\frac{\sigma}{\rho r_c}} \tag{13}$$

For the present problem, Equation (13) indicates $u_c > 0$ to account for multidroplets coalescence induced jumping. Jumping velocity u_c is increased by increasing N, matching the conclusion by Kim et al.[42] Thus, our functional metal heterogeneous surface is also helpful for surface self-cleaning, and preventing ice formation in cold weather.

The above results are for the heterogeneous surface generated by mesh screen of PPI = 240, where PPI means the number of pores per inch. To verify the effectiveness of the present method, another heterogeneous surface was made by mesh screen of PPI = 400 (see Figure S6, Supporting Information, for micro/nanostructure). Nanostructure does not depend on mesh screen size, but microdot size is apparently decreased to $a = 18$ µm, $b = 14$ µm. P is decreased to 90 µm. The decrease of P generates more droplets in a specific area by condensing wet air. Similarly, droplet pattern is not good when the surface is horizontally positioned. The vertically arranged surface creates perfect droplets array (see Figure S7, Supporting Information). The droplet density is 121 mm^{-2}, which is almost three times of that on the surface generated by mesh screen of PPI = 240.

3. Comments on the Present Method and Finding

To fabricate heterogeneous surface, conventional lithography method is used with the help of a mask.[14,18] Initially, a uniform hydrophobicity surface is prepared. Then, selective etching generates hydrophilic island/cavity arrays.[15,20] The prepared heterogeneous surface has sufficient resolution benefitted from high accuracy of MEMS fabricated mask. The prepared surface area is limited by mask size and fabrication cost, thus it cannot be large. Recently, atomic force microscope or femtosecond

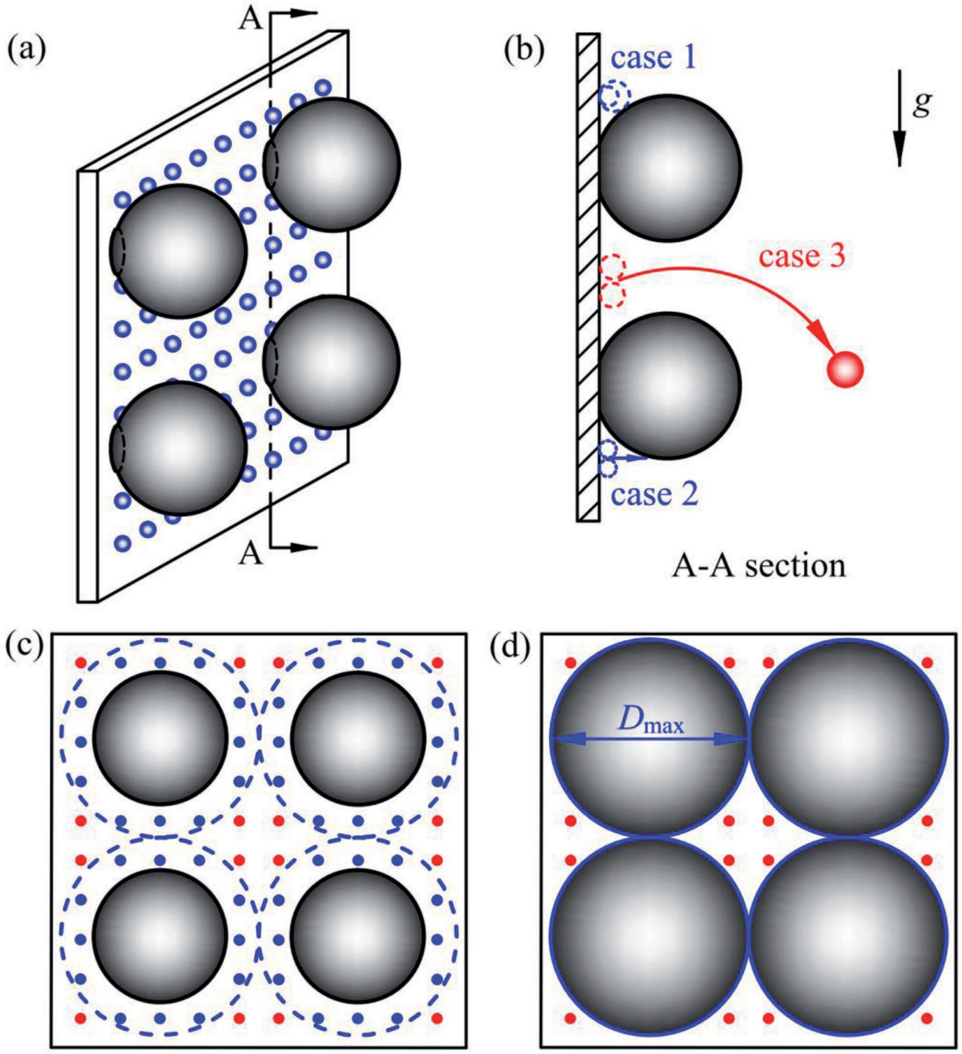

Figure 8. Interactions between neighboring droplet and main droplet to explain perfect main droplets array: a) coexistence of neighboring and main droplets; b) three cases for neighboring droplets dynamics; c) equal possibility of neighboring droplets captured by main droplets; d) maximum main droplet diameter limited by hydrophilic dots distance.

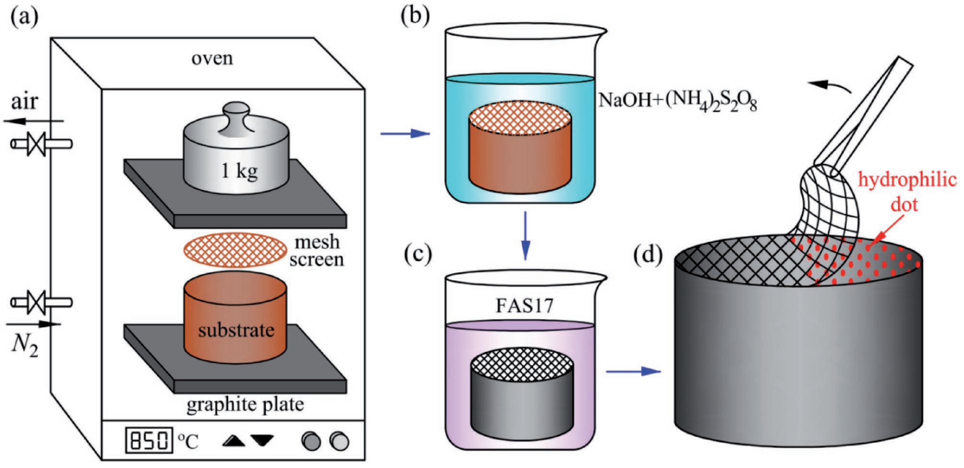

Figure 9. Three steps to fabricate heterogeneous (hydrophilic/hydrophobic) surface: a) diffusion welding in oven; b,c) chemical treatment for superhydrophobicity; d) separating mesh screen from copper substrate to expose microhydrophilic dots.

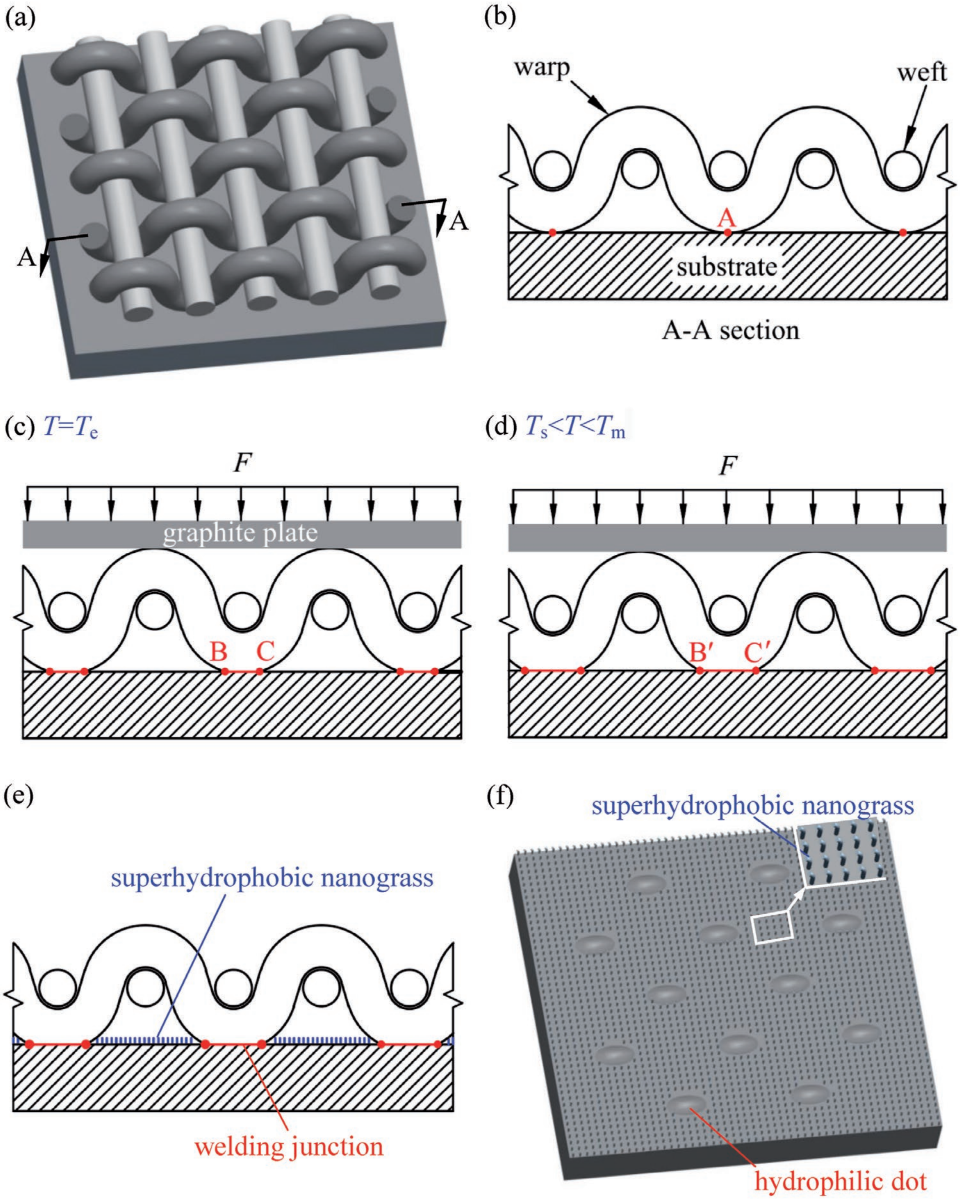

Figure 10. The principle to form heterogeneous surface: a) mesh screen on metal substrate; b) point contact array forms between mesh screen and copper; c) dot contact array forms by applying an external force; d) welding junction array forms by diffusion welding; e) chemical treatment forms hydrophobic structure; f) heterogeneous surface is formed after tearing mesh screen from metal surface.

laser are also proposed to create heterogeneous surface.[48,49] The common characteristic of the above methods is the small surface size and relatively high cost. These surfaces can be applied in electronic, optical, or biology engineering. Here, a hydrophilic/superhydrophobic surface is created combining mesh screen and diffusion welding technique. Because mesh screen is commercialized with low cost, and diffusion welding technique is mature for industry applications, our metal heterogeneous surface is cost effective for large scale utilization such as heat exchangers and dust particle collection by fine droplets.

Many methods are available to grow nanostructure on surface. The major contribution of this paper is to form hydrophilic microdots arrays on metal substrate, belonging to the nonsilicon micromachining. For this method, the distance between neighboring hydrophilic microdots is $P = \sqrt{2}(w+d)$, where w is the pore width and d is the mesh wire thickness. With PPI = 400, P can be 90 µm, which is almost the finest size for commercial mesh screen product. Microdot size is ≈10 µm scale, depending on geometrical parameters of mesh screen and external force applied on mesh screen. The size resolution of heterogeneous surface is in ≈1 µm, which is acceptable for large scale utilization.

This is the preliminary work using welding technique and mesh screen to create heterogeneous surface. This method can be extended for such surface formation on other metal substrates. This extension depends on suitable matches of materials of mesh screen and metal substrate. Mesh screens of copper (Cu), nickel (Ni), molybdenum (Mo), titanium (Ti) and stainless steel are available commercially. For example, titanium mesh screen can be welded on one of the following metal substrates: copper,[50] steel,[51] and nickel.[52] Fabrication of heterogeneous surface on these metal surfaces is recommended to be continued.

4. Conclusions

Mesh screen is used as mask and diffusion welding technique is introduced. Diffusion welding technique creates "welding junction array." Chemical treatment of sintered package generates nanostructures to behave hydrophobicity except welding junctions. Tearing mesh screen from copper surface exposes hydrophilic dots to form hydrophilic/hydrophobic surface.

Droplet array is not perfect on horizontal surface. When a returning droplet impacts a main droplet, the merged droplet may induce stabilization without jumping, single time jumping, multitimes jumping (domino effect), rotating or billiard effect induced jumping, explaining the not perfect droplets array. A theoretical analysis using nondimensional parameters was performed to explain if a merged droplet can jump and why jumping velocity can be larger than impacting velocity for specific condition.

Droplets array is perfect on vertical surface. For neighboring droplets not under main droplets, the merged neighboring droplet departs without returning. For neighboring droplets under main droplets, they are captured by main droplets, and the capture possibilities are identical for different main droplets. Our heterogeneous surface paves a new road for large scale nonsilicon micromachining. Perfect droplets array can be generated by controllable dropwise condensation, for various functions such as fine particle collecting and electromagnetic wave absorption etc.

5. Experimental Section

Three steps for fabrication of heterogeneous surface were involved: (1) welding junction array formation by the diffusion welding technique in an oven (**Figure 9**a); (2) nanosurface modification by chemical solutions (Figure 9b,c); and (3) separating mesh screen from copper substrate to expose hydrophilic dot array (Figure 9d). The detailed fabrication of the heterogeneous surface can be seen in the Supporting Information.

Figure 10 describes the fabrication principle. Mesh screen consists of straight weft wires and curved warp wires (see Figure 10a). Due to its perfectly periodic structure, "point contact array" is formed when one puts a mesh screen on a plain surface (see point A in Figure 10b). At an environment temperature of T_e, when an external force F is applied uniformly on mesh screen, the "point contact array" is extended to form "dot contact array," due to weak deformation of warp wires (see dot BC in Figure 10c). The small amount of specific element in mesh wires slightly decreases melting temperature compared with pure metal substrate. Sintering the bonded package in an oven at high temperature melts the "dot contact array." Oven temperature should be controlled in a range between softening temperature T_s and melting temperature T_m. At the desired oven temperature, dot BC is extended to dot B′C′ (see Figure 10d). After decreasing oven temperature, melting areas are solidified to form welding junction array. The method is called diffusion welding technique in metallurgy industry. Chemical treatment of the sintered package generates nanostructure on metal surface except welding junction array. The welding junction prevents such area from exposing in chemical solution (see Figure 10e). Removing mesh screen from metal surface leaves microdot array. Figure 10f shows hydrophilic microdot array among superhydrophobic nanostructure, yielding the heterogeneous surface. The hydrophilic microdot array exactly corresponds to the welding junction array shown in Figure 10e.

It is difficult to characterize wettabilities of nanograss area and microdot. A novel method was developed for contact angle (CA) measurement. Another sample was prepared, half with a solid film cover and the left without a film cover. The cover material was identical to mesh screen. Similar welding, chemical treatment, and separating processes were performed. CA was measured on the two half parts independently. The superhydrophobic part had a static CA of 154.7°, advancing CA of 162°, and rolling angle of less than 2°. The other part had a static CA of 45.3° and advancing CA of 73.9° to display hydrophilic nature. The CA of 154.7° corresponds to nanograss area in Figure 1c and the value of 45.3° corresponds to microdot area in Figure 1d.

Supporting Information

Supporting Information is available from the Wiley Online Library or from the author.

Acknowledgements

This work was supported by the National Natural Science Foundation of China with Contract No. 51436004.

Conflict of Interest

The authors declare no conflict of interest.

Keywords

diffusion welding, droplet array, dropwise condensation, heterogeneous surface, mesh screen

Received: June 12, 2017
Revised: August 12, 2017

---

[1] V. G. Damle, X. D. Sun, K. Rykaczewski, *Adv. Mater. Interface* **2015**, *2*, 1500202.
[2] B. S. Sikarwar, S. Khandekar, K. Muralidhar, *Sādhanā* **2013**, *38*, 1135.
[3] B. S. Sikarwar, S. Khandekar, S. Adrawal, S. Kumar, K. Muralidhar, *Heat Transfer Eng.* **2012**, *33*, 301.
[4] M. F. Mei, B. M. Yu, J. C. Cai, L. Luo, *Int. J. Heat Mass Transfer* **2009**, *52*, 4823.
[5] A. R. Liberski, J. T. Delaney Jr., U. S. Schubert, *ACS Comb. Sci.* **2011**, *13*, 190.
[6] Y. Zhu, Y. X. Zhang, W. W. Liu, Y. Ma, Q. Fang, B. Yao, *Sci. Rep.* **2015**, *5*, 9551.
[7] J. Ziauddin, D. M. Sabatini, *Nature* **2001**, *411*, 107.
[8] R. Lino, Y. Matsumoto, K. Nishino, A. Yamaguchi, H. Noji, *Front. Microbiol.* **2013**, *4*, 300.
[9] A. I. Neto, C. R. Correia, C. A. Custódio, J. F. Mano, *Adv. Funct. Mater.* **2014**, *24*, 5096.

[10] S. Grilli, L. Miccio, V. Vespini, A. Finizio, S. De Nicola, P. Ferraro, *Opt. Express* **2008**, *16*, 8084.
[11] D. J. Won, S. Baek, H. Kim, J. Kim, *Sensor. Actuators, A* **2015**, *235*, 151.
[12] A. A. Popova, S. M. Schillo, K. Demir, E. Ueda, A. Nesterov-Mueller, P. A. Levkin, *Adv. Mater.* **2015**, *27*, 5217.
[13] L. Mishchenko, J. Aizenberg, B. D. Hatton, *Adv. Funct. Mater.* **2013**, *23*, 4577.
[14] K. Tadanaga, J. Morinaga, A. Matsuda, T. Minami, *Chem. Mater.* **2000**, *12*, 590.
[15] W. Q. Feng, L. X. Li, E. Ueda, J. S. Li, S. Heißler, A. Welle, O. Trapp, P. A. Levkin, *Adv. Mater. Interface* **2014**, *1*, 1400269.
[16] K. Nakata, S. Nishimoto, Y. Yuda, T. Ochiai, T. Murakami, A. Fujishima, *Langmuir* **2010**, *26*, 11628.
[17] R. D. Sun, A. Nakajima, A. Fujishima, T. Watanabe, K. Hashimato, *J. Phys. Chem. B* **2001**, *105*, 1984.
[18] S. Costacurta, P. Falcaro, L. Malfatti, D. Marongiu, B. Marmiroli, F. Cacho-Nerin, H. Amenitsch, N. Kirkby, P. Innocenzi, *Langmuir* **2011**, *27*, 3898.
[19] T. Balgar, S. Franzka, E. Hasselbrink, N. Hartman, *Appl. Phys. A: Mater.* **2006**, *82*, 15.
[20] J. J. Bowen, J. M. Taylor, C. P. Jurich, S. A. Morin, *Adv. Funct. Mater.* **2015**, *25*, 5520.
[21] E. Ölçeroğlu, M. Mccarthy, *ACS Appl. Mater. Interfaces* **2016**, *8*, 5729.
[22] Y. J. Yoo, S. Ju, S. Y. Park, Y. J. Kim, J. Bong, T. Lim, K. W. Kim, J. Y. Rhee, Y. Lee, *Sci. Rep.* **2015**, *5*, 14018.
[23] Z. W. Zuo, J. F. Wang, Y. P. Huo, H. L. Liu, R. B. Xu, *Environ. Eng. Sci.* **2016**, *33*, 650.
[24] J. Zhang, Q. Shen, G. Q. Luo, M. J. Li, L. M. Zhang, *Mater. Des.* **2012**, *39*, 81.
[25] T. Gietzelt, V. Toth, A. Huell, F. Messerschmidt, R. Dittmeyer, *Adv. Eng. Mater.* **2014**, *16*, 1381.
[26] B. X. Liu, L. J. Huang, L. Geng, B. Wang, C. Liu, W. C. Zhang, *J. Alloys Compd.* **2014**, *602*, 187.
[27] X. M. Dai, F. H. Yang, R. G. Yang, Y.-C. Lee, C. Li, *Int. J. Heat Mass Transfer* **2013**, *64*, 1101.
[28] M. Y. Cao, J. S. Xiao, C. M. Yu, K. Li, L. Jiang, *Small* **2015**, *11*, 4379.
[29] Z. J. Cheng, C. Li, H. Lai, Y. Du, H. W. Liu, M. Liu, K. N. Sun, L. G. Jin, N. Q. Zhang, L. Jiang, *Adv. Mater. Interfaces* **2016**, *3*, 1600370.
[30] H. Li, M. Y. Cao, X. Y. Ma, Y. X. Zhang, X. Jin, K. S. Liu, L. Jiang, *Adv. Mater. Interfaces* **2016**, *3*, 1600276.
[31] R. Enright, N. Miljkovic, J Sprittles, K. Nolan, R. Mitchell, E. N. Wang, *ACS Nano* **2014**, *8*, 10352.
[32] X. M. Chen, J. A. Weibel, S. V. Garimella, *Adv. Mater. Interface* **2015**, *2*, 1400480.
[33] F. C. Wang, F. Q. Yang, Y. P. Zhao, *Appl. Phys. Lett.* **2011**, *98*, 053112.
[34] N. Miljkovic, R. Enright, Y. S. Nam, K. Lopez, N. Dou, J. Sack, E. N. Wang, *Nano Lett.* **2013**, *13*, 179.
[35] M. He, X. Zhou, X. P. Zeng, D. P. Cui, Q. L. Zhang, J. Chen, H. L. Li, J. J. Wang, Z. X. Cao, Y. L. Song, L. Jiang, *Soft Matter* **2012**, *8*, 6680.
[36] J. Liu, H. Y. Guo, B. Zhang, S. S. Qiao, M. Z. Shao, X. R. Zhang, X.-Q. Feng, Q. Y. Li, Y. L. Song, L. Jiang, J. J. Wang, *Angew. Chem., Int. Ed.* **2016**, *55*, 4265.
[37] J. B. Boreyko, C. H. Chen, *Phys. Rev. Lett.* **2009**, *103*, 184501.
[38] K. Rykaczwski, A. T. Paxson, S. Anand, X. M. Chen, Z. K. Wang, K. Varanasi, *Langmuir* **2013**, *29*, 881.
[39] Y. T. Luo, J. Li, J. Zhu, Y. Zhao, X. F. Gao, *Angew. Chem., Int. Ed.* **2015**, *54*, 4876.
[40] C. J. Lv, P. F. Hao, Z. H. Yao, Y. Song, X. W. Zhang, F. He, *Appl. Phys. Lett.* **2013**, *103*, 021601.
[41] X. L. Liu, P. Cheng, X. J. Quan, *Int. J. Heat Mass Trans.* **2014**, *73*, 195.
[42] M. K. Kim, H. Cha, P. Birbarah, S. Chavan, C. Zhong, Y. H. Xu, N. Miljkovic, *Langmuir* **2015**, *31*, 13452.
[43] X. M. Chen, R. S. Patel, J. A. Weibel, S. V. Garimella, *Sci. Rep.* **2016**, *6*, 18649.
[44] Y. M. Hou, M. Yu, X. M. Chen, Z. K. Wang, S. H. Yao, *ACS Nano* **2015**, *9*, 71.
[45] C. J. Lv, P. F. Hao, Z. H. Yao, F. L. Niu, *Langmuir* **2015**, *31*, 2414.
[46] A. Aili, H. X. Li, M. H. Alhosani, T. J. Zhang, presented at *The ASME 5th Int. Conf. on Micro/Nanoscale Heat Mass Transfer, Biopolis*, Singapore, January **2016**.
[47] F. Xing, J. L. Xu, J. Xie, H. Liu, Z. X. Wang, X. L. Ma, *Int. J. Multiphase Flow* **2015**, *71*, 98.
[48] F. F. Wang, P. Li, D. Wang, L. H. Li, S. X. Xie, L. Q. Liu, Y. C. Wang, W. J. Li, *Sci. Rep.* **2014**, *4*, 6524.
[49] M. Moura, E. Teodori, A. S. Moita, A. L. N. Moreira, Y. Bai, X. L. Li, Y. Liu, presented at *The 5th Int. Conf. Bionic Eng.*, Ningbo, China **2016**.
[50] K. Aydın, Y. Kaya, N. Kahraman, *Mater. Des.* **2012**, *37*, 356.
[51] L. Kolařík, M. Kolaříková, P. Vondrouš, *Key Eng. Mater.* **2013**, *586*, 178.
[52] X. Shao, X. L. Guo, Y. F. Han, W. J. Lu, J. N. Qin, D. Zhang, *Mater. Des.* **2015**, *65*, 1001.